ÓPTICA PURA Y APLICADA
www.sedoptica.es

Type: RESEARCH PAPER
Section: BIOPHOTONICS/MEDICAL OPTICS

Determining light absorption changes in multilayered turbid media through analytically computed photon mean partial pathlengths

Determinación de cambios de absorción de la luz en medios turbios multicapas a través del cálculo analítico de los caminos parciales medios fotónicos

D. A. Vera[1*], H. A. García[1], M. V. Waks-Serra[1], N. A. Carbone[1], D. I. Iriarte[1], J. A Pomarico[1]

1. IFAS-CIFICEN (UNCPBA - CICPBA - CONICET)

(*) E-mail: dvera@ifas.exa.unicen.edu.ar S: miembro de SEDOPTICA / SEDOPTICA member

Received: 20/04/2023 Accepted: 16/06/2023
DOI: 10.7149/OPA.56.2.51145

ABSTRACT:

In this work we introduce a model for analytically computing the mean partial pathlengths (MPPLs) of photons in optically turbid media consisting in an arbitrary number of layers, being the deepest one infinitely thick. This has several applications in the field of Biomedical Optics, especially when modelling light propagation in biological tissues and systems such as the human head. The computational implementation of our model surpasses the current state-of-the-art calculations done by means of Monte Carlo (MC) simulations, which, despite their robustness, represent a bottleneck in terms of computation times and hardware requirements when real-time applications are considered. In order to validate the approach presented in this work, we compared it with MPPLs generated by MC simulations for turbid layered media with different numbers of layers and several combinations of optical properties and thicknesses. Results show a very good agreement between theory and simulations, with relative errors of less than 10% having place mainly in the first layer. It is expected that this investigation contributes to increasing the accuracy of the models currently used for studying light propagation in highly heterogeneous biological tissues.

Key words: fNIRS, Multilayered Media, Mean Partial Pathlengths, Monte Carlo Simulations

RESUMEN:

En este trabajo presentamos un modelo para el cálculo analítico de los caminos parciales medios (MPPLs) de fotones en medios ópticamente turbios formados por un número arbitrario de capas, siendo la última infinitamente gruesa. Esto tiene numerosas aplicaciones en el campo de la Óptica Biomédica, especialmente al modelar la propagación de la luz en tejidos y sistemas biológicos como la cabeza humana. La implementación computacional de nuestro modelo supera el estado del arte de los cálculos actuales realizados mediante simulaciones de Monte Carlo (MC), las cuales, a pesar de su robustez, representan un cuello de botella en términos de tiempos de cómputo y de requisitos de hardware al momento de considerar aplicaciones en tiempo real. Con el fin de validar el modelo presentado en este trabajo, comparamos nuestro método con los MPPLs generados por simulaciones de MC para medios turbios multicapas con diferentes números de capas y diferentes combinaciones de propiedades ópticas y de espesores. Los resultados muestran un muy buen acuerdo entre teoría y simulaciones, con errores relativos menores al 10% que tienen lugar principalmente en la primera capa. Se espera que esta investigación contribuya a aumentar la precisión de los modelos actualmente usados para estudiar la propagación de la luz en tejidos biológicos altamente heterogéneos.

Palabras clave: fNIRS, Medios Multicapas, Caminos Parciales Medios, Simulaciones de Monte Carlo

REFERENCES AND LINKS / REFERENCIAS Y ENLACES

[1] F. Jöbsis, "Noninvasive, infrared monitoring of cerebral and myocardial oxygen sufficiency and circulatory parameters," Science **198**, 1264-1267 (1977).

[2] A. P. Gibson, J. C. Hebden, S. R. Arridge, "Recent advances in diffuse optical imaging," Phys. Med. Biol. **50**(4), R1-R43 (2005).

[3] F. Scholkmann, S. Kleiser, A. J. Metz, R. Zimmermann, J. M. Pavia, U. Wolf, M. Wolf, "A review on continuous wave functional near-infrared spectroscopy and imaging instrumentation and methodology," NeuroImage **85**, 6-27 (2014).

[4] A. Torricelli, D. Contini, A. Pifferi, M. Caffini, R. Re, L. Zucchelli, L. Spinelli, "Time domain functional NIRS imaging for human brain mapping," NeuroImage **85**, 28-50 (2014).

[5] L. Hou, Y. Liu, L. Qian, Y. Zheng, J. Gao, W. Cao, Y. Shang, "Portable near-infrared technologies and devices for noninvasive assessment of tissue hemodynamics," J. Health. Eng. **2019**, 3750495 (2019).

[6] A. Cheung, L. Tu, A. Macnab,B. K. Kwon, B. Shadgan, "Detection of hypoxia by near-infrared spectroscopy and pulse oximetry: a comparative study," J. Biomed. Opt. **27**(7), 077001 (2022).

[7] G. Quarto, L. Spinelli, A. Pifferi, A. Torricelli, R. Cubeddu, F. Abbate, N. Balestreri, S. Menna, E. Cassano, P. Taroni, "Estimate of tissue composition in malignant and benign breast lesions by time-domain optical mammography," Biomed. Opt. Expr. **5**(10), 3684-3698 (2014).

[8] B. Montcel, R. Chabrier, P. Poulet, "Detection of cortical activation with time-resolved diffuse optical methods," App. Opt. **44**(10), 1942-1947 (2005).

[9] T. Fischer, B. Ebert, J. Voigt, R. Macdonald, U. Schneider, A. Thomas, B. Hamm, K.-G. A. Hermann, "Detection of rheumatoid arthritis using non-specific contrast enhanced fluorescence imaging," Acad. Radiol. **17**, 375 (2010).

[10] M. Patterson, B. Chance, B. Wilson, "Time resolved reflectance and transmittance for the non-invasive measurement of tissue optical properties," Appl. Opt. **28**, 2331-2336 (1989).

[11] A. Ishimaru, "Diffusion of light in turbid material," Appl. Opt. **28**, 2210-2215 (1989).

[12] D. Contini, F. Martelli, G. Zaccanti, "Photon migration through a turbid slab described by a model based on diffusion approximation. I. Theory," Appl. Opt. **36**(19), 4587-4599 (1997).

[13] S. Jacques, "Optical properties of biological tissues: a review," Phys. Med. Biol. **58**, 37-61 (2013).

[14] J. Steinbrink, H. Wabnitz, H. Obrig, A. Villringer, H. Rinneberg, "Determining changes in NIR absorption using a layered model of the human head," Phys. Med. Biol. **46**, 879-896 (2001).

[15] L. Zucchelli, D. Contini, R. Re, A. Torricelli, L. Spinelli, "Method for the discrimination of superficial and deep absorption variations by time domain fNIRS," Biomed. Opt. Expr. **4**(12), 2893-2910 (2013).

[16] D. Boas, C. Elwell, M. Ferrari, G. Taga, "Twenty years of functional near-infrared spectroscopy: introduction for the special issue," NeuroImage **85**, 1-5 (2014).

[17] A. Jelzow, H. Wabnitz, I. Tachtsidis, E. Kirilina, R. Brühl, R. Macdonald, "Separation of superficial and cerebral hemodynamics using a single distance time-domain NIRS measurement", Biomed. Opt. Expr. **5**(5), 1465-1482 (2014).

[18] T. Huppert, S. Diamond, M. Franceschini, D. Boas, "Homer: a review of time-series analysis methods for near-infrared spectroscopy of the brain," Appl. Opt. **48**(10), D280–D298 (2009).

[19] F. Fabbri, A. Sassaroli, M. E. Henry, S. Fantini, "Optical measurements of absorption changes in two-layered diffusive media," Phys. Med. Biol. **49**, 1183–1201 (2004).

[20] R. B. Saager, A. J. Berger, "Direct characterization and removal of interfering absorption trends in two-layer turbid media," J. Opt. Soc. Am. A **22**, 1874–1882 (2005).

[21] M. Hiraoka, M. Firbank, M. Essenpreis, M. Cope, S. Arridge, P. van der Zee, D. Delpy, "A Monte Carlo Investigation of optical pathlength in inhomogeneous tissue and its application to near-infrared spectroscopy," Phys. Med. Biol. **38**, 1859-1876 (1993).

[22] H. A. García, D. A. Vera, M. V. W. Serra, G. R. Baez, D. I. Iriarte, J. A. Pomarico, "Theoretical investigation of photon partial pathlengths in multilayered turbid media," Biomed. Opt. Expr. **13**, 2516–2529 (2022).

[23] S. Del Bianco, F. Martelli, G. Zaccanti, "Penetration depth of light re-emitted by a diffusive medium: theoretical and experimental investigation," Phys. Med. Biol. **47**, 4131-4144 (2002).

[24] F. Martelli, S. Del Bianco, A. Ismaelli, G. Zaccanti, Light propagation through biological tissue and other diffusive media: theory, solutions and software. Washington, SPIE Press (2010).

[25] H. A. García, D. I. Iriarte, J. A. Pomarico, D. Grosenick, R. Macdonald, "Retrieval of the optical properties of a semi infinite compartment in a layered scattering medium by single-distance, time-resolved diffuse reflectance measurements," J. Quant. Spectrosc. Radiat. Transfer **189**, 66-74 (2017).

[26] Q. Fang and S. Yan, "Graphics processing unit-accelerated mesh-based Monte Carlo photon transport simulations," J. Biomed. Opt. **24**, 115002 (2019).

[27] T. Vo-Dinh (Ed.), Biomedical Photonics Handbook, Boca Raton, CRC Press (2003).

[28] A. Kienle, S. Patterson, N. Dögnitz, R. Bays, G. Wagniéres, H. van den Bergh, "Non-invasive determination of the optical properties of two-layered turbid media," Appl. Opt. **37**(4), 779-791 (1998).

[29] B. Hallacoglu, A. Sassaroli, S. Fantini, "Optical characterization of two-layered turbid media for non-invasive, absolute oximetry in cerebral and extracerebral tissue," PLoS ONE **8**(5), 1-15 (2013).

[30] F. Martelli, S. Del Bianco, G. Zaccanti, "Procedure for retrieving optical properties of a two-layered medium from time-resolved reflectance measurements," Opt. Lett. **28**(14), 1236-1238 (2003).

[31] A. Liebert, H. Wabnitz, J. Steinbrink, H. Obrig, M. Möller, R. Macdonald, A. Villringer, H. Rinneberg, "Time-resolved multidistance near-infrared spectroscopy of the adult head: intracerebral and extracerebral absorption changes from moments of distribution of times of flight of photons," Appl. Opt. **43**(15), 3037-3047 (2004).

[32] D. A. Vera, H. A. García, M. V. Waks-Serra, N. A. Carbone, D. I. Iriarte, J. A. Pomarico, "Reconstruction of light absorption changes in the human head using analytically computed photon partial pathlengths in layered media," J. Opt. Soc. Am. A **40**(4), C126-C137 (2023).

1. Introduction

During the last decades, Near InfraRed Spectroscopy (NIRS) has gained increasing attention in the Biomedical Optics community due to its ability to sense in a non-invasively way inner regions of living tissue with relatively low-cost and portable devices [1-5]. Among its applications we can find tissue oximetry [6], optical mammography [7], brain haemodynamics [8] and rheumatoid arthritis [9], to mention but a few, and sometimes with the additional possibility of implementing these technologies in real time [3,4].

The theory of light diffusion in highly scattering media can be applied to this type of problems to extract useful information from the detected signal [10-13], which can provide valuable insights regarding tissue oxygenation, chromophores concentration, structural information such as the presence of inhomogeneities and so on [13].

Regarding the experimental procedures, NIRS techniques usually require the coupling of a pair of optical fibres to the skin of the subject under study; one of them serves as a NIR light source, while the other one works as a detector, which collects the photons diffusively reflected by the explored tissue [10]. Under NIR illumination, biological tissues behave as highly scattering turbid media and can be characterised mainly by three parameters, namely the absorption coefficient, μ_a, the reduced scattering coefficient, μ'_s, and the refractive index, n. In the particular case of studying brain haemodynamics, one of the main metrics used to evaluate the presence or absence of activation in the cortex is the attenuation A as a function of the wavelength λ and the source-detector distance ρ, which can be computed by means of the Modified Beer-Lambert law (MBLL) [3]:

$$A(\rho,\lambda) = -\log\left(\frac{I(\rho,\lambda)}{I_0(\rho,\lambda)}\right) = L(\rho,\lambda)\Delta\mu_a(\lambda), \quad (1)$$

where $L(\rho,\lambda)$ is the mean partial pathlength (MPPL) of photons inside the tissue, and $\Delta\mu_a(\lambda)$ is the absorption change that produces the variation in light intensity $I(\rho,\lambda)$ with respect to the reference signal $I_0(\rho,\lambda)$. The cause for these absorption changes is none other than changes in chromophores concentrations; in the field of functional NIRS (fNIRS), for which the main goal is to determine which region (or regions) of the brain is (are) activated in response to a given motor or cognitive task, two main chromophores are usually considered, namely oxyhaemoglobin (HbO) and deoxyhaemoglobin (HbR), so $\Delta\mu_a$ can be obtained as follows [3,4]:

$$\Delta\mu_a(\lambda) = \varepsilon_{HbO}(\lambda)\Delta[HbO] + \varepsilon_{HbR}(\lambda)\Delta[HbR], \quad (2)$$

being ε_{HbO} (ε_{HbR}) the molar extinction coefficient of HbO (HbR) at wavelength λ. In Eq. (2), the square brackets in [*HbO*] and [*HbR*] represent concentrations.

Equations (1) and (2) together represent the model used to study variations in the detected light signal when changes in [*HbO*] and [*HbR*] take place in biological tissues such as the human head. As it must already be noted by the reader (particularly through Eq. (1)), this model accounts only for homogeneous turbid media, i.e., those for which the optical parameters are the same throughout the whole volume. The reason for this is that the reconstruction process is much easier than for the case where heterogeneities are considered [14]; this can be seen, for example, in the computation of the MPPLs for homogeneous media, which can be analytically computed in a number of situations [12].

However, biological systems like the human head are far from being optically homogeneous. Instead, a more natural way of modelling light propagation in such types of tissues are layered turbid media, where each layer has its own set of optical parameters. This requires the following modification to Eq. (1):

$$A(\rho,\lambda) = \sum_{j=1}^{N} L_j(\rho,\lambda)\,\Delta\mu_{a,j}(\rho,\lambda), \tag{3}$$

where N is the total number of layers in the medium and j is the index representing each layer. Of course, a change in the absorption of layer j is now due to its own combination of changes in oxy- and deoxyhaemoglobin, i.e., $\Delta[HbO]_j$ and $\Delta[HbR]_j$.

Regarding the fNIRS technique applied to the human brain, chromophore concentration changes of interest are mostly focused in the grey matter region [14-17], which, in sight of the complex structure of the human head, evidently makes the homogeneous models rather inappropriate. Moreover, contributions to these changes from more superficial layers can mask or even block the desired changes in the cortex. In order to account for these inaccuracies, a number of strategies have been adopted. For example, the homogeneous MPPL in Eq. (1) can be expressed as a product of the source-detector distance ρ, a *differential pathlength factor* (DPF) and a *partial volume correction* (PVC) factor, which are intended to scale lengths such as to represent only the distance travelled by photons in the turbid volume corresponding to the grey matter [18]. This approach can be combined with the use of the so-called short detector channels (SDCs), which consists in source-detector pairs separated by a distance $\rho_S \sim$ 5-15 mm [3], allowing the collection of information at the surface, which can then be subtracted from the overall signal A given by Eq. (1); this procedure retains only information coming from deeper regions of the studied medium [3,19,20].

Although these methods perform better than the homogeneous models alone, they still pose some problems. In principle, quantities such as the DPF and the PVC must be taken as constant independently of the human subject under consideration and the type and place of the brain activation [18], something which in general is far from being true. As well as this, the use of SDCs alone introduce undesired crosstalk between the upper and the deeper zones being explored by light [19,20].

Up to date, the only way to compute the MPPLs in layered media, as the human head, was by means of Monte Carlo (MC) simulations [14,15,21], since it is impossible to experimentally determine them for an anatomically representative geometry of it. However, this approach generally requires highly demanding hardware capabilities and takes long computation times, preventing the retrieval of oxy- and deoxyhaemoglobin changes in real time experiments. Recently, some of the authors have developed a method to analytically compute the MPPLs in turbid media consisting of up to four flat layers (a simplified human head model) in a few milliseconds [22]. Of course this model is still far from the extremely complex anatomical description, but it can be justified by three main reasons: i) due to the highly diffusive nature of the medium under study, the detailed structure of the model is not of utmost importance, ii) it outperforms the homogeneous model approach, allowing to naturally separate the chromophore concentration changes occurring in the layer of interest (grey matter) from those taking place outside it and iii) real time experiments are now feasible.

In this way we have been able to demonstrate that the MPPLs strongly depend on the optical properties of each layer, as well as on its thicknesses and on the source-detector separation ρ, something which remains neglected when using homogeneous models. Our method allows for increasing the specificity of the information retrieved from each layer and also decreases the crosstalk between them.

In this work we present an improvement of our own method by which analytical MPPLs can be directly computed for diffusive media with an arbitrary number of layers. This permits an even higher increase in the specificity of each layers' information, allowing to model tissue types usually packed together, such as the meninges, or even studying the penetration depth of photons for different source-detector arrays. The

time consumption remains bounded to a few milliseconds, which makes the approach still feasible for real time applications. Comparison with MC simulations show an excellent agreement, with errors of less than 10%.

This manuscript is organised as follows: Section 2 introduces the theoretical concepts needed to analytically compute the MPPLs in a layered turbid medium with an arbitrary number of layers; Section 3 shows the details of the MC simulations run for comparison purposes; Section 4 presents the main results of this work; and finally, the corresponding conclusions together with plausible future lines of work are discussed in Section 5.

2. Theory

As previously established by several works [15,21,23,24], the MPPLs of photons in layer j (j = 1, 2, ..., N) in an N-layered turbid medium can be calculated using the following equation:

$$L_j(\rho,\lambda) = -\frac{1}{R(\rho,\lambda)}\frac{\partial R(\rho,\lambda)}{\partial \mu_{a_j}}, \tag{4}$$

being $R(\rho, \lambda)$ the diffuse reflectance measured at a distance ρ from the source emitting light at wavelength λ and impinging at the top surface of the turbid medium. It is possible to feed Eq. (4) with any analytical model representing $R(\rho,\lambda)$ and then perform its corresponding derivatives to obtain an analytical expression for $L_j(\rho,\lambda)$.

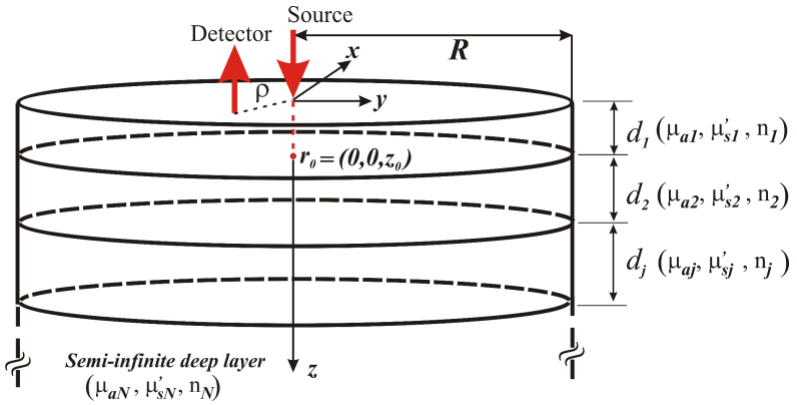

Fig. 1. Schematic representation of a multilayered turbid medium with a semiinfinite deepest layer. A pencil like beam impinges onto the top layer at coordinates (x,y,z) =(0,0,0), which can be modelled by an isotropic source located at r_0= (0,0,z_0=1/$\mu'_{s,1}$) inside the first layer. The diffusively reflected light is collected at the same surface and at a distance ρ from the source.

To this end, we can assume a schematic configuration as the one shown by Fig. 1. The turbid medium of interest (such as the human head in our case) is assumed to be formed by a stack of layers (each of them with optical properties $\mu_{a,j}$, $\mu'_{s,j}$ and n_j) of finite thicknesses d_j, except for the last one, which is semiinfinite. All the layers are separated by planar interfaces (a fair assumption if we keep ρ much smaller than the radius of the head). Under this configuration, it can be demonstrated that the $R(\rho,\lambda)$ takes the form [25]:

$$R(\rho,\lambda) = \frac{1}{4A(\pi R_{EB})^2}\sum_{n=1}^{\infty} G_1(z=0;s_n,\boldsymbol{\mu})\frac{J_0(s_n\rho)}{{J_1}^2(s_n R_{EB})}, \tag{5}$$

Here, A is a factor that accounts for the refractive index mismatch between the turbid medium and the environment; R_{EB} is the extrapolated radius for which the photon fluence satisfies the extrapolated boundary condition [12]; J_0 and J_1 are the Bessel functions of the first species and of orders 0 and 1, respectively; $G_1(z = 0;s_n,\boldsymbol{\mu})$ is the Green's function for layer 1 (where the source is placed); s_n are rescaled Bessel zeros, such that $J_0(s_n R_{EB}) = 0$; and $\boldsymbol{\mu} = (\mu_1, \mu_2, ..., \mu_j, ..., \mu_N)$, where $\boldsymbol{\mu}_j$ summarises the collection of optical parameters and thicknesses of layer j. Two things must be noted here: i) a pencil beam source (like the one represented in Fig. 1) becomes completely isotropic at a depth $z_0 = 1/\mu'_{s,1}$ when the medium is highly

scattering [10,11]; and ii) as stated in Eqs. (1)-(3), the dependence of the reflectance with λ takes place solely by means of the absorption coefficients $\mu_{a,j}$, which have been omitted in expression (5) for the sake of clarity.

In order to compute the MPPLs given by expression (4), the explicit form of the Green's function G_1 is needed:

$$G_1(z=0;s_n,\boldsymbol{\mu}) = \frac{\exp(-\alpha_1 z_0) - \exp\left[-\alpha_1\left(z_0+2z_{b,1}\right)\right]}{2D_1\alpha_1} \times \frac{\sinh\left[\alpha_1\left(z_0+z_{b,1}\right)\right]\sinh\left[\alpha_1 z_{b,1}\right]}{D_1\alpha_1\exp\left[\alpha_1\left(d_1+z_{b,1}\right)\right]} \times \\ \times \frac{D_1\alpha_1 n_1^2\beta_3 - D_2\alpha_2 n_2^2\gamma_3}{D_1\alpha_1 n_1^2\cosh\left[\alpha_1\left(d_1+z_{b,1}\right)\right]\beta_3 + D_2\alpha_2 n_2^2\sinh\left[\alpha_1\left(d_1+z_{b,1}\right)\right]\gamma_3}, \tag{6}$$

being $z_{b,1}$ the extrapolated surface in the z direction (equivalent to R_{EB} in the radial direction); $D_j = 1/3\mu'_{s,j}$, while α_j are quantities given by:

$$\alpha_j = \sqrt{\frac{\mu_{a,j}}{D_j} + {s_n}^2}. \tag{7}$$

Besides, β_3 and γ_3 are factors obtained by recursion relations, beginning with β_N and γ_N:

$$\beta_N = D_{N-1}\alpha_{N-1}{n_{N-1}}^2\cosh[\alpha_{N-1}d_{N-1}] + D_N\alpha_N{n_N}^2\sinh[\alpha_{N-1}d_{N-1}], \\ \gamma_N = D_{N-1}\alpha_{N-1}{n_{N-1}}^2\sinh[\alpha_{N-1}d_{N-1}] + D_N\alpha_N{n_N}^2\cosh[\alpha_{N-1}d_{N-1}], \tag{8}$$

And then "going down" to $k = 4$ as follows:

$$\beta_{k-1} = D_{k-2}\alpha_{k-2}{n_{k-2}}^2\cosh[\alpha_{k-2}d_{k-2}]\,\beta_k + D_{k-1}\alpha_{k-1}{n_{k-1}}^2\sinh[\alpha_{k-2}d_{k-2}]\,\gamma_k, \\ \gamma_{k-1} = D_{k-2}\alpha_{k-2}{n_{k-2}}^2\sinh[\alpha_{k-2}d_{k-2}]\,\beta_k + D_{k-1}\alpha_{k-1}{n_{k-1}}^2\cosh[\alpha_{k-2}d_{k-2}]\,\gamma_k. \tag{9}$$

Details about how these relations hold can be found in Ref. [25].

Equation (4) indicates that we need the derivatives of $R(\rho,\lambda)$ with respect to each $\mu_{a,j}$, which reduces to the calculation of the derivatives of G_1:

$$\frac{\partial R(\rho,\lambda)}{\partial\mu_{a,j}} = \frac{1}{4A(\pi R_{EB})^2}\sum_{n=1}^{\infty}\frac{G_1(z=0;s_n,\boldsymbol{\mu})}{\partial\mu_{a,j}}\frac{J_0(s_n\rho)}{{J_1}^2(s_n R_{EB})}. \tag{10}$$

Since the different absorption coefficients act through the parameter α_j, the derivatives of G_1 can be computed as:

$$\frac{\partial\alpha_1(z=0;s_n,\boldsymbol{\mu})}{\partial\mu_{a,j}} = \frac{G_1(z=0;s_n,\boldsymbol{\mu})}{\partial\alpha_j}\times\frac{\partial\alpha_j}{\partial\mu_{a,j}}. \tag{11}$$

By means of relation (7) we can easily see that:

$$\frac{\partial\alpha_j}{\partial\mu_{a,j}} = \frac{1}{2D_j\alpha_j}. \tag{12}$$

Now we proceed by splitting G_1 as defined in expression (6) in the following manner:

$$G_1 = {G_1}^I + G_1^{II}\times G_1^{III}, \tag{13}$$

with:

$$G_1{}^{I} = \frac{\exp(-\alpha_1 z_0) - \exp\left[-\alpha_1\left(z_0 + 2z_{b,1}\right)\right]}{2D_1\alpha_1},$$

$$G_1{}^{II} = \frac{\sinh\left[\alpha_1\left(z_0 + z_{b,1}\right)\right]\sinh\left[\alpha_1 z_{b,1}\right]}{D_1\alpha_1\exp\left[\alpha_1\left(d_1 + z_{b,1}\right)\right]}, \tag{14}$$

$$G_1{}^{III} = \frac{\delta}{\Delta};$$

where:

$$\delta = D_1\alpha_1 n_1^2\beta_3 - D_2\alpha_2 n_2^2\gamma_3,$$
$$\Delta = D_1\alpha_1 n_1^2\cosh\left[\alpha_1\left(d_1 + z_{b,1}\right)\right]\beta_3 + D_2\alpha_2 n_2^2\sinh\left[\alpha_1\left(d_1 + z_{b,1}\right)\right]\gamma_3; \tag{15}$$

these definitions will facilitate the forthcoming reading and calculus. We can begin by writing the derivative of G_1 with respect to a α_1:

$$\frac{\partial G_1}{\partial\alpha_1} = \frac{\partial G_1^I}{\partial\alpha_1} + \frac{G_1^{II}}{\partial\alpha_1}\times G_1^{III} + G_1{}^{II}\times\frac{G_1^{III}}{\partial\alpha_1}. \tag{16}$$

The derivatives of $G_1{}^{I}$, $G_1{}^{II}$ and $G_1{}^{III}$ with respect to α_1 are:

$$\frac{\partial G_1^I}{\partial\alpha_1} = \frac{\exp\left[-\alpha_1\left(z_0 + 2z_{b,1}\right)\right]\left[\alpha_1\left(z_0 + 2z_{b,1}\right) + 1\right] - \exp[-\alpha_1 z_0]\,(-\alpha_1 z_0)(z_0\alpha_1 + 1)}{2D_1\alpha_1^2}, \tag{17}$$

$$\frac{\partial G_1^{II}}{\partial\alpha_1} = \Big(\Big\{\left(z_0 + z_{b,1}\right)\cosh\left[\alpha_1\left(z_0 + z_{b,1}\right)\right]\sinh\left[\alpha_1 z_{b,1}\right] + z_{b,1}\sinh\left[\alpha_1\left(z_0 + z_{b,1}\right)\right]\cosh\left[\alpha_1 z_{b,1}\right]\Big\}\alpha_1$$
$$- \sinh\left[\alpha_1\left(z_0 + z_{b,1}\right)\right]\sinh\left(\alpha_1 z_{b,1}\right)\left[1 + \alpha_1\left(d_1 + z_{b,1}\right)\right]\Big)\frac{1}{D_1\alpha_1^2\exp\left[\alpha_1\left(d_1 + z_{b,1}\right)\right]}, \tag{18}$$

$$\frac{\partial\, G_1^{III}}{\partial\,\alpha_1} = \frac{\partial G_1^{III}}{\partial\delta}\frac{\partial\delta}{\partial\alpha_1} + \frac{\partial G_1^{III}}{\partial\Delta}\frac{\partial\Delta}{\partial\alpha_1} = \frac{1}{\Delta}\frac{\partial\delta}{\partial\alpha_1} - \frac{\delta}{\Delta^2}\frac{\partial\Delta}{\partial\alpha_1}, \tag{19}$$

with:

$$\frac{\partial\delta}{\partial\alpha_1} = D_1\, n_1\,\beta_3, \tag{20}$$

$$\frac{\partial\Delta}{\partial\alpha_1} = \left[D_1 n_1{}^2\beta_3 + \left(d_1 + z_{b,1}\right)D_2\alpha_2 n_2^2\gamma_3\right]\cosh\left[\alpha_1\left(d_1 + z_{b,1}\right)\right] +$$
$$\left(d_1 + z_{b,1}\right)D_1\alpha_1 n_1^2\beta_3\sinh\left[\alpha_1\left(d_1 + z_{b,1}\right)\right]. \tag{21}$$

Note that, by virtue of the recursion relations (9), expression (21) shows no derivatives of β_3 and γ_3 with respect to α_1.

Next, we can write the derivatives of G_1 with respect to α_j being $j > 1$:

$$\frac{\partial G_1}{\partial \alpha_j} = G_1^{II} \times \frac{\partial G_1^{III}}{\partial \alpha_j}. \tag{22}$$

Although this expression seems easier to compute than its counterpart (16), in this case we will have nonzero derivatives of β_j and γ_j, which implies the appearance of new recursion relations. Here it is convenient to begin by deriving β_N and γ_N with respect to α_N:

$$\begin{aligned} \frac{\partial \beta_N}{\partial \alpha_N} &= D_N n_N^2 \sinh(\alpha_{N-1} d_{N-1}), \\ \frac{\partial \gamma_N}{\partial \alpha_N} &= D_N n_N^2 \cosh(\alpha_{N-1} d_{N-1}). \end{aligned} \tag{23}$$

We can now do the same with β_{N-1} and γ_{N-1}:

$$\begin{aligned} \frac{\partial \beta_{N-1}}{\partial \alpha_N} &= D_{N-2}\alpha_{N-2} n_{N-2}^2 \cosh(\alpha_{N-2} d_{N-2}) \frac{\partial \beta_N}{\partial \alpha_N} + D_{N-1}\alpha_{N-1} n_{N-1}^2 \sinh(\alpha_{N-2} d_{N-2}) \frac{\partial \gamma_N}{\partial \alpha_N} \\ \frac{\partial \gamma_{N-1}}{\partial \alpha_N} &= D_{N-2}\alpha_{N-2} n_{N-2}^2 \sinh(\alpha_{N-2} d_{N-2}) \frac{\partial \beta_N}{\partial \alpha_N} + D_{N-1}\alpha_{N-1} n_{N-1}^2 \cosh(\alpha_{N-2} d_{N-2}) \frac{\partial \gamma_N}{\partial \alpha_N} \end{aligned} \tag{24}$$

Note that, as $\beta_k = \beta_k(\alpha_{k-1}, \alpha_k, \dots, \alpha_N)$ and $\gamma_k = \gamma_k(\alpha_{k-1}, \alpha_k, \dots, \alpha_N)$:

$$\frac{\partial \beta_k}{\partial \alpha_j} = \frac{\partial \gamma_k}{\partial \alpha_j} = 0 \quad \text{for} \quad j \leq k - 2.$$

From here on, we can continue deriving with respect to α_N until we reach the derivatives of β_3 and γ_3. However, at some point the intermediate derivatives of β_j and γ_j begin to nest together, so we still need the following expressions to complete the set of "starting points":

$$\begin{aligned} \frac{\partial \beta_N}{\partial \alpha_{N-1}} &= D_{N-1} n_{N-1}^2 \cosh(\alpha_{N-1} d_{N-1}) + (D_{N-1}\alpha_{N-1} n_{N-1}^2 + D_N \alpha_N n_N^2) d_{N-1} \sinh(\alpha_{N-1} d_{N-1}), \\ \frac{\partial \gamma_N}{\partial \alpha_{N-1}} &= D_{N-1} n_{N-1}^2 \sinh(\alpha_{N-1} d_{N-1}) + (D_{N-1}\alpha_{N-1} n_{N-1}^2 + D_N \alpha_N n_N^2) d_{N-1} \cosh(\alpha_{N-1} d_{N-1}). \end{aligned} \tag{25}$$

Given all this, we are in conditions of deriving the recursion relations (9) with respect to any α_k:

$$\begin{aligned} \frac{\partial \beta_{j-1}}{\partial \alpha_k} &= \left[D_{j-2} n_{j-2}^2 \left(\frac{\partial \alpha_{j-2}}{\partial \alpha_k} \beta_j + \alpha_{j-2} \frac{\partial \beta_j}{\partial \alpha_k} \right) + \frac{\partial \alpha_{j-2}}{\partial \alpha_k} d_{j-2} D_{j-1} \alpha_{j-1} n_{j-1}^2 \gamma_j \right] \cosh(\alpha_{j-2} d_{-2}) \\ &\quad + \left[D_{j-1} n_{j-1}^2 \left(\frac{\partial \alpha_{j-1}}{\partial \alpha_k} \gamma_j + \alpha_{j-1} \frac{\partial \gamma_j}{\partial \alpha_k} \right) + \frac{\partial \alpha_{j-2}}{\partial \alpha_k} d_{j-2} D_{j-2} \alpha_{j-2} n_{j-2}^2 \beta_j \right] \sinh(\alpha_{j-2} d_{-2}), \\ \frac{\partial \gamma_{j-1}}{\partial \alpha_k} &= \left[D_{j-2} n_{j-2}^2 \left(\frac{\partial \alpha_{j-2}}{\partial \alpha_k} \beta_j + \alpha_{j-2} \frac{\partial \beta_j}{\partial \alpha_k} \right) + \frac{\partial \alpha_{j-2}}{\partial \alpha_k} d_{j-2} D_{j-1} \alpha_{j-1} n_{j-1}^2 \gamma_j \right] \sinh(\alpha_{j-2} d_{-2}) \\ &\quad + \left[D_{j-1} n_{j-1}^2 \left(\frac{\partial \alpha_{j-1}}{\partial \alpha_k} \gamma_j + \alpha_{j-1} \frac{\partial \gamma_j}{\partial \alpha_k} \right) + \frac{\partial \alpha_{j-2}}{\partial \alpha_k} d_{j-2} D_{j-2} \alpha_{j-2} n_{j-2}^2 \beta_j \right] \cosh(\alpha_{j-2} d_{-2}). \end{aligned} \tag{26}$$

These new recursion relations are completely general and rely upon three possible different conditions on the derivatives of α_m (which do not occur simultaneously):

$$\frac{\partial \alpha_{j-2}}{\partial \alpha_k} = \delta_{j-2,k},$$
$$\frac{\partial \alpha_{j-1}}{\partial \alpha_k} = \delta_{j-1,k}, \qquad (27)$$
$$\frac{\partial \alpha_{j-2}}{\partial \alpha_k} = \frac{\partial \alpha_{j-1}}{\partial \alpha_k} = 0 \quad (k \geq j),$$

Where $\delta_{m,k}$ is the Kronecker's delta.

With all this, we are finally capable of computing the MPPLs as expressed by Eq. (4). As a last remark for this Section, we can mention that the mean total pathlength of photons throughout the whole medium is easily computed as the sum of all the mean partial pathlengths in each layer:

$$L_{TOT}(\rho, \lambda) = \sum_{j=1}^{N} L_j(\rho, \lambda). \qquad (28)$$

3. Monte Carlo simulations

In order to validate our model, MC simulations were performed to compute the MPPLs for layered media consisting of different numbers of layers. To this end we made use of MCX, a Matlab toolkit implemented in the CUDA architecture [26]. The simulations were run on a server with an 11th generation CPU Intel Core i7-11370H at 3.30 GHz × 8, 64 GB RAM, and a GPU NVIDIA GeForce RTX 3050 Mobile. For each simulation, 8×10^8 photons were launched in a 3D turbid medium of 220 × 220 × 100 mm^3 (voxel size of 1 mm^3), taking an average time of 60 s.

In all cases, different combinations of optical parameters were chosen in the range of the typical values found in biological tissues [27], as well as different thicknesses for each layer, so as to have a wide set of situations to be compared with the model introduced in the previous Section. Then, for each situation a total of twenty simulations were run, from which average values of the MPPLs were obtained, together with the corresponding standard deviations. Regarding the source-detector distance ρ, a total of twelve values were selected, ranging from 5 mm to 60 mm, with an isotropic point source placed at r = (0, 0, z_0=1/$\mu'_{s,1}$) and detectors with a diameter of 0.5 mm. Unless otherwise stated, the refractive index of each layer was always set to n = 1.33; this choice is supported by the high water content of the modelled tissues.

4. Results

Our very first study regards the behaviour of the layered model introduced in Section 2 when all the layers have the same optical properties, which in turn implicitly represents a homogeneous medium. To this end, we have run MC simulations for "homogenised" two-, three-, four- and five-layered media, and compared the corresponding MPPLs as a function of the source-detector distance ρ with the outcomes from our model. The results are shown in Figs. 2 to 5 (upper rows). As it can be seen, the matching is in all cases excellent. As stated at the end of Section 2, the mean total pathlengths can be computed by summing up all the partial pathlengths. These results are shown in the corresponding lower rows of each of Figs. 2 to 5; here we have also added the results predicted by the homogeneous model [12]. The coincidence between the three methods is, once again, perfect. It is important to notice that, although the mean total pathlengths for the two-, three-, four- and five-layered medium are obtained by a summation over a different number of terms (with increasing complexity as the number of layers also increases), the final result is always the same.

Although in principle there is no point in making use of a complex layered model when a homogeneous medium is involved, here we can claim that the layered model provides additional information regarding intermediate regions of the whole volume, and this is more evident as the number of layers increases.

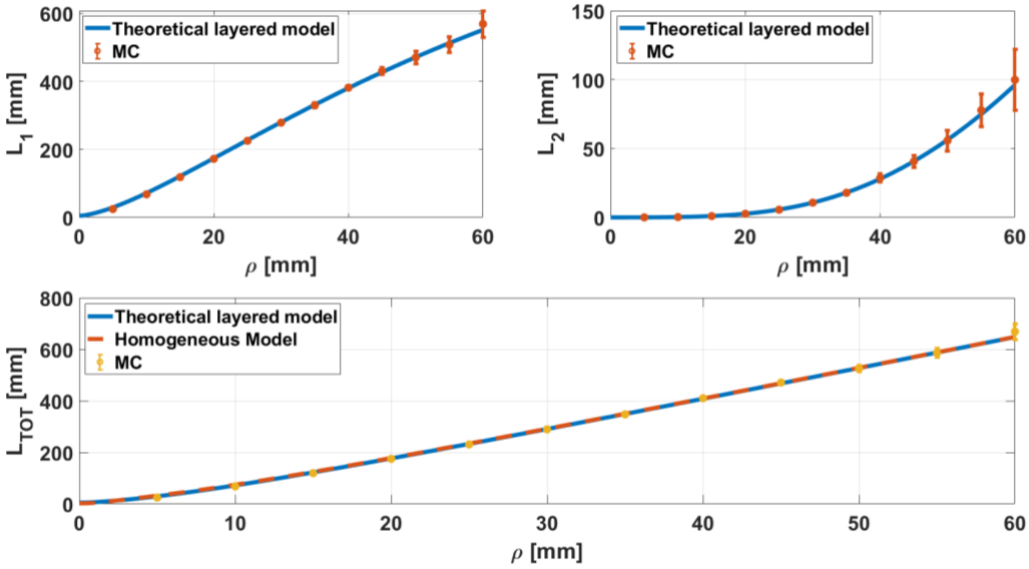

Fig. 2. Comparison (as a function of the source-detector distance ρ) between MC simulations and the analytical model of Section 2 for a two-layered medium, with optical properties $\mu_{a,1} = \mu_{a,2} = 0.005$ mm^{-1} and $\mu'_{s,1} = \mu'_{s,2} = 1$ mm^{-1}, and the thickness of the first layer being $d_1 = 20$ mm. Top: MPPLs in layer 1 (L_1, left) and in layer 2 (L_2, right). Bottom: mean total pathlength (L_{TOT}) computed as the sum of the partial pathlengths L_1 and L_2; for comparison purposes, here L_{TOT} as predicted by the homogeneous model is also shown.

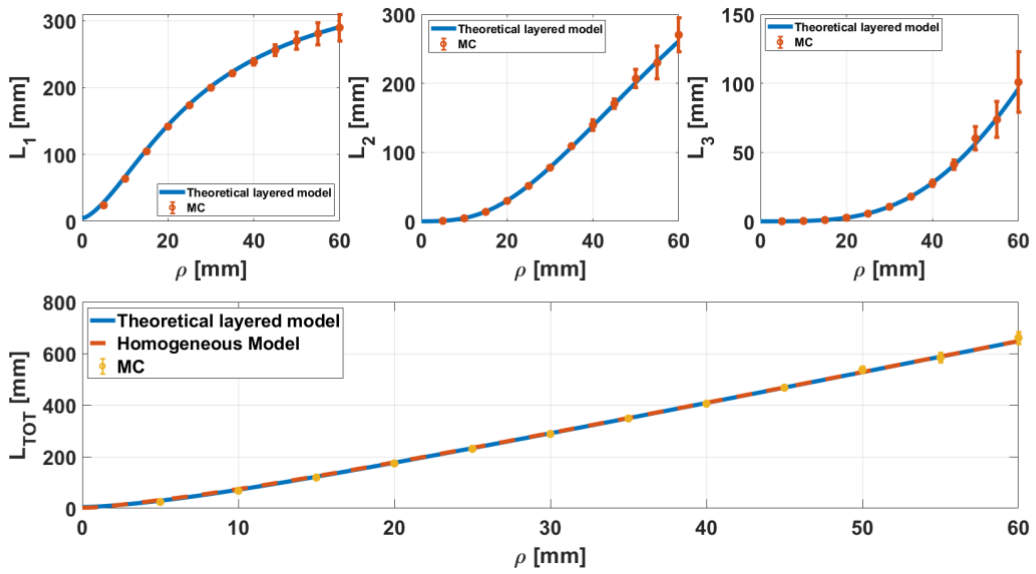

Fig. 3. Comparison (as a function of the source-detector distance ρ) between MC simulations and the analytical model of Section 2 for a three-layered medium, with optical properties $\mu_{a,1} = \mu_{a,2} = \mu_{a,3} = 0.005$ mm^{-1} and $\mu'_{s,1} = \mu'_{s,2} = \mu'_{s,3} = 1$ mm^{-1}, and the thicknesses of the first two layers being $d_1 = d_2 = 10$ mm. Top: MPPLs in layer 1 (L_1, left), in layer 2 (L_2, centre) and in layer 3 (L_3, right). Bottom: mean total pathlength (L_{TOT}) computed as the sum of the partial pathlengths L_1, L_2 and L_3; for comparison purposes, here L_{TOT} as predicted by the homogeneous model is also shown.

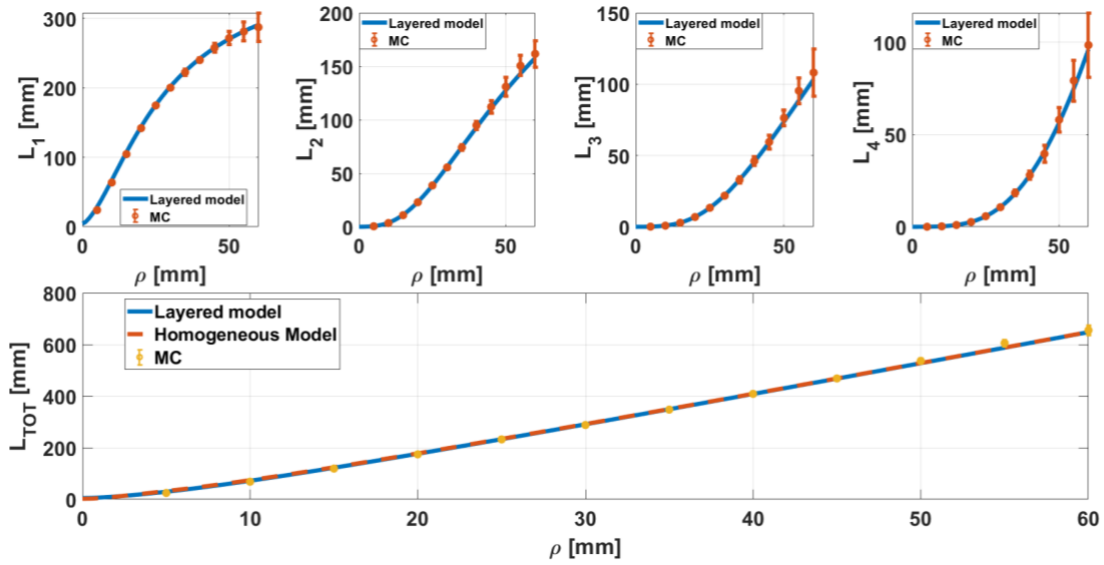

Fig. 4. Comparison (as a function of the source-detector distance ρ) between MC simulations and the analytical model of Section 2 for a four-layered medium, with optical properties $\mu_{a,1} = \mu_{a,2} = \mu_{a,3} = \mu_{a,4} = 0.005$ mm^{-1} and $\mu'_{s,1} = \mu'_{s,2} = \mu'_{s,3} = \mu'_{s,4} = 1$ mm^{-1}, and the thicknesses of the first three layers being $d_1 = 10$ mm and $d_2 = d_3 = 5$ mm. Top: from left to right, MPPLs in layer 1 (L_1), in layer 2 (L_2), in layer 3 (L_3) and in layer 4 (L_4). Bottom: mean total pathlength (L_{TOT}) computed as the sum of the partial pathlengths L_1, L_2, L_3 and L_4; for comparison purposes, here L_{TOT} as predicted by the homogeneous model is also shown.

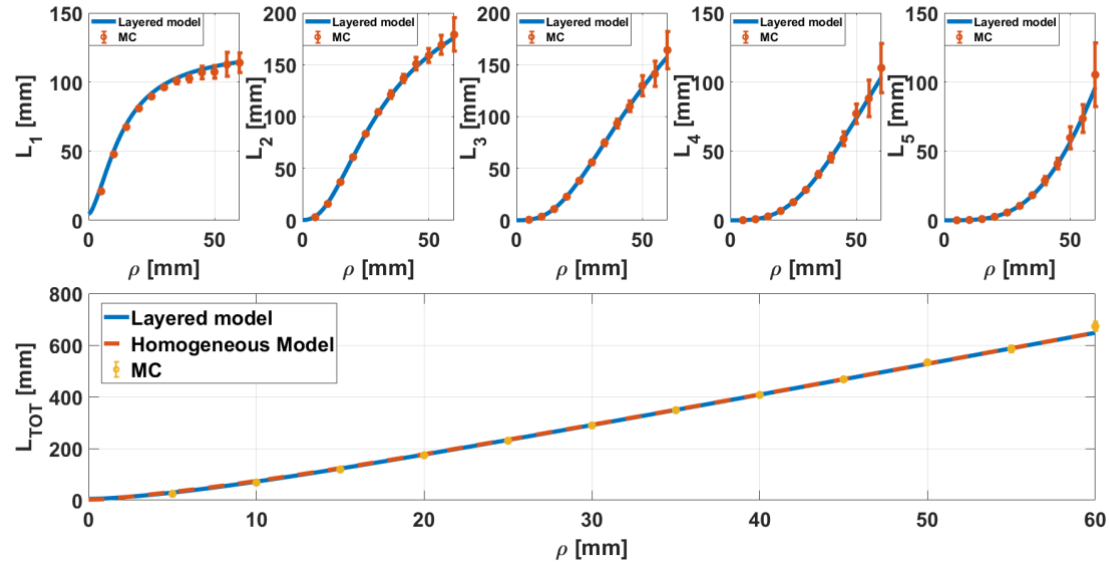

Fig. 5. Comparison (as a function of the source-detector distance ρ) between MC simulations and the analytical model of Section 2 for a five-layered medium with optical properties $\mu_{a,1} = \mu_{a,2} = \mu_{a,3} = \mu_{a,4} = \mu_{a,5} = 0.005$ mm^{-1} and $\mu'_{s,1} = \mu'_{s,2} = \mu'_{s,3} = \mu'_{s,4} = \mu'_{s,5} = 1$ mm^{-1}, and the thicknesses of the first four layers being $d_1 = d_2 = d_3 = d_4 = 5$ mm. Top: from left to right, MPPL in layer 1 (L_1), in layer 2 (L_2), in layer 3 (L_3), in layer 4 (L_4) and in layer 5 (L_5). Bottom: mean total pathlength (L_{TOT}) computed as the sum of the partial pathlengths L_1, L_2, L_3, L_4 and L_5; for comparison purposes, here L_{TOT} as predicted by the homogeneous model is also shown.

Next, we test our model for heterogeneous layered media. Figure 6 shows another comparison between MC and the layered model for a ten-layered medium; detailed information regarding the absorption and reduced scattering coefficients can be found in the caption. This time the comparison is excellent for all layers except for the first one, where we can notice small discrepancies (< 5%) for values of ρ > 25 mm. These differences can be explained by the fact that, for large source-detector separations combined with a small thickness of the first layer, the vast majority of the photons launched in the MC simulations travels almost directly to the lower layers of the medium before entering the diffusive regime; however, our model is entirely based on the diffusion theory [10-12], which means the upper layer needs appropriate combinations of optical and geometrical parameters in order to fulfil the conditions required for the

diffusive regime to hold (something that is not completely guaranteed in the particular case shown here). This hypothesis is supported by the results shown in the previous figures (where not only $\mu_{a,1} \ll \mu'_{s,1}$, as needed in order to satisfy the diffusive regime, but also the thickness of the first layer is large enough in all cases).

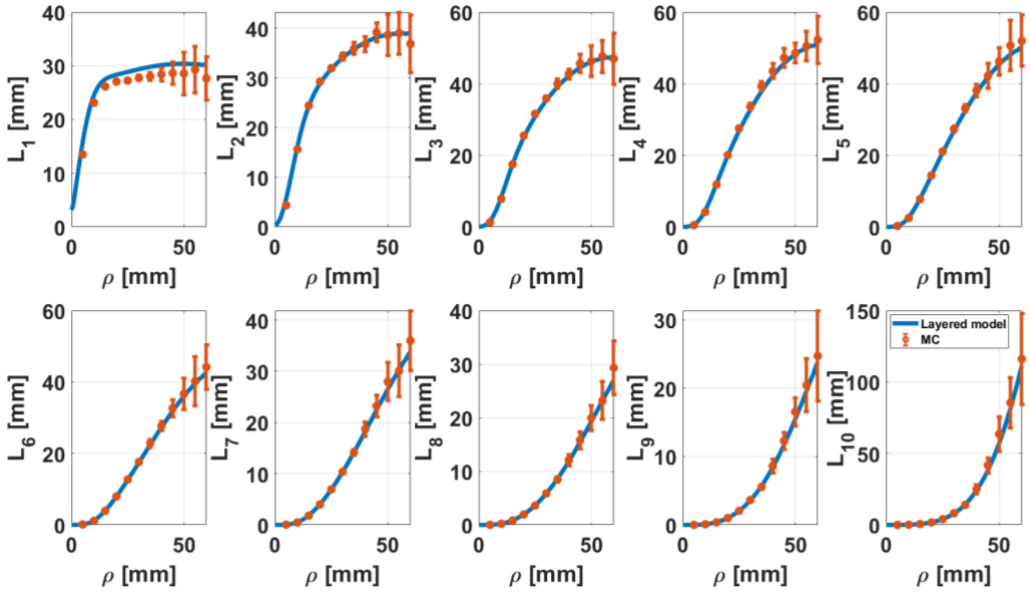

Fig. 6. Comparison (as a function of the source-detector distance ρ) between MC simulations and the analytical model of Section 2 for a ten-layered medium, with optical properties $\boldsymbol{\mu}_a$ = (0.002, 0.020, 0.010, 0.0160, 0.004, 0.008, 0.0140, 0.0180, 0.0120, 0.006) mm^{-1} and $\boldsymbol{\mu'}_s$ = (1.20, 1.12, 0.81, 0.50, 0.88, 0.96, 0.73, 1.04, 0.57, 0.65) mm^{-1}, and d_i = 2 mm, with i = 1, ..., 9.

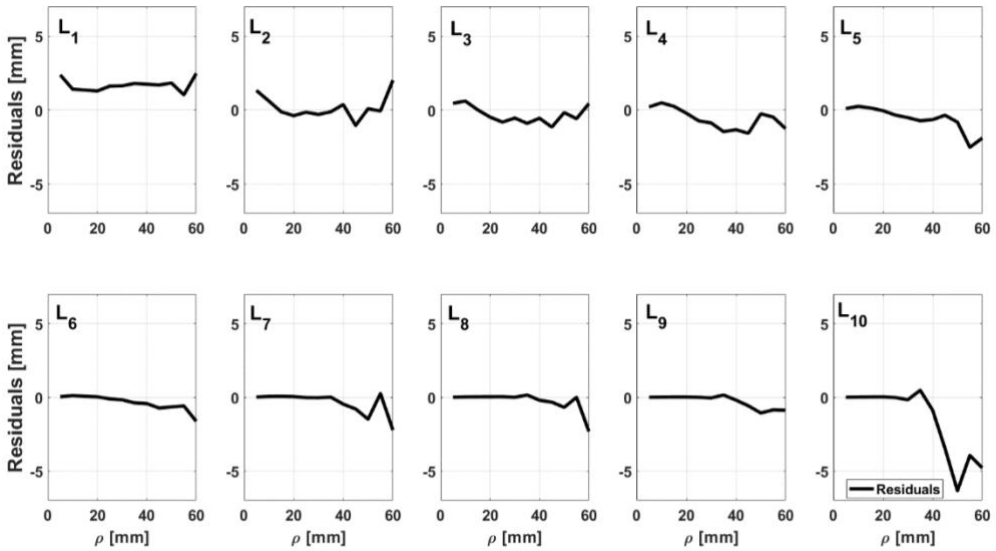

Fig. 7. Residuals obtained by subtracting the analytical MPPLs and the MC simulated MPPLs for the ten-layered case.

Fig. 7 shows the residuals of the comparison between the theoretical approach and the MC simulations that correspond to Fig. 6. Here, the largest differences (below 10 %) are found in the first and last layers; in the first case the reason for this has already been discussed in the previous paragraph, while in the latter, this can be explained by the low photon count for such long source-detector separations.

Another interesting comparison is shown in Fig. 8, also for the previously described ten-layered medium, but this time as a function of the depth *z*. The matching between theory and MC is still very good, except once again for depths of $z \sim 2$ mm, which represent the interface between layers 1 and 2; this difference is consistent with the explanation given in the preceding paragraph. Here it can be noted that the sensitivity

of photons to depth (taken as the peak of each curve shown in the Figure) increases with the source-detector distance, something in accordance with all the findings reported in the literature [28-30]. As a last remark regarding Fig. 8., we can add that this representation of our results is equivalent to that present in [31] under the label of Fig. 3 (although in the latter case obtained solely by means of MC simulations for a homogeneous medium), but here we have had the advantage of being able to compute the MPPLs in just a matter of a few milliseconds.

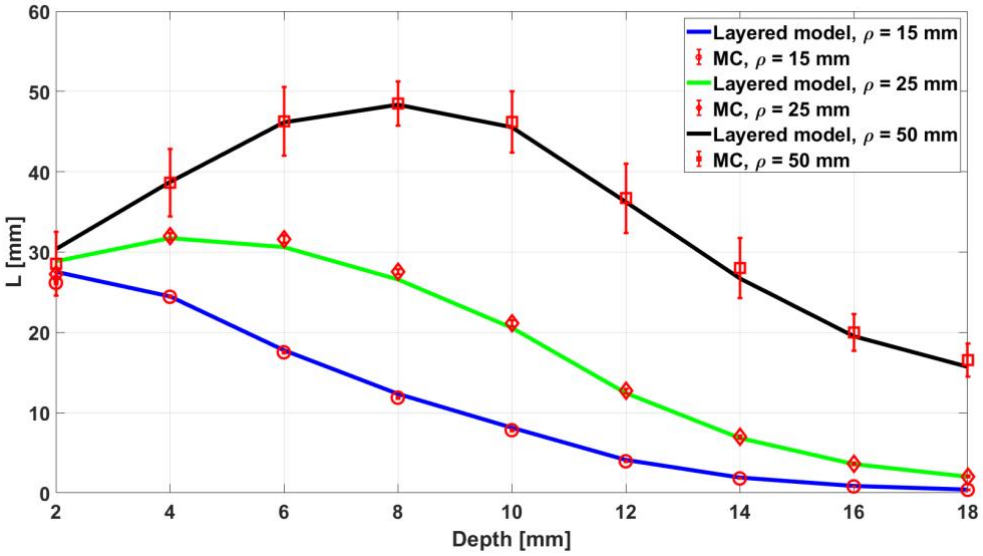

Fig. 8. Comparison between MC simulations and the MPPLs (as a function of the depth z) obtained by our analytical model for the ten-layered medium shown in Fig. 6 and for three different source-detector distances, namely ρ = 15 mm, ρ = 25 mm and ρ = 50 mm.

The dependence of the MPPLs with ρ can in principle be inferred from Fig. 6; however, and having already found a fair agreement between MC and theory, we can gather all the analytical MPPLs together in one single plot, as shown in Fig. 9. Here it can be clearly seen that the MPPL in layer 1 saturates for values of ρ > 10 mm, and this behaviour tends to be mimicked by the subsequent layers with the increase in the source-detector separation until we reach the bottom layer, which finds no bounds in its increase (a reasonable conclusion given that it has a semiinfinite extension). The Fig. **9** described below is equivalent to that present in **[14]** under the label of Fig. **2** (again, the Figure we are referring to was obtained by means of MC simulations for a homogeneous medium); as mentioned before, our theory greatly improves the computation times compared to MC. In fact, the computation times needed to obtain the MPPLs analytically in a twenty-layered medium are in the order of 10 to 100 milliseconds. On the other hand, each of the twenty corresponding MC simulations run took about 60 seconds to be done, so in order to obtain the MPPLs, with a standard deviation of, at most, 30 %, a total computation time of ~1200 seconds is needed. Not to mention that these MC simulation times were obtained using a CUDA-parallelized code, which needs at least one GPU to run. CPU-based versions of the same MC programs are much slower. On the contrary, the codes needed to compute the MPPLs in an analytically manner can be run under much less restrictive conditions in almost any modern PC.

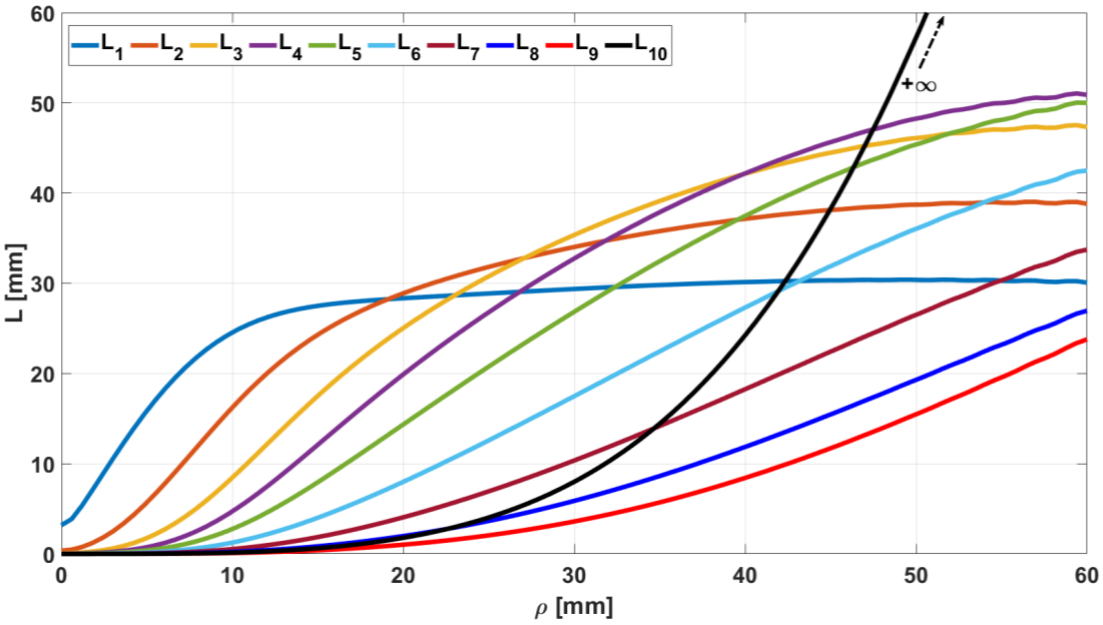

Fig. 9. Analytical MPPLs for the ten-layered medium shown in Fig. 6, plotted altogether as a function of the source-detector separation ρ.

Finally, we replicate the results shown in Figs. 6, 7, 8 and 9 but now for a twenty-layered medium (Figs. 10, 11, 12 and 13). Although this does not necessarily represent a practical situation, it is worth mentioning that the calculation of each and every mean partial pathlength is still possible regardless of neither the time consumption nor the statistics based on the detected photons (something which, in turn, is inherent in the nature of Monte Carlo simulations). In particular, Fig. 9 shows a very nice agreement between MC and theory except, again, for the first layer, this time with differences below 10%, something reasonable considering the rather small thickness of the layer.

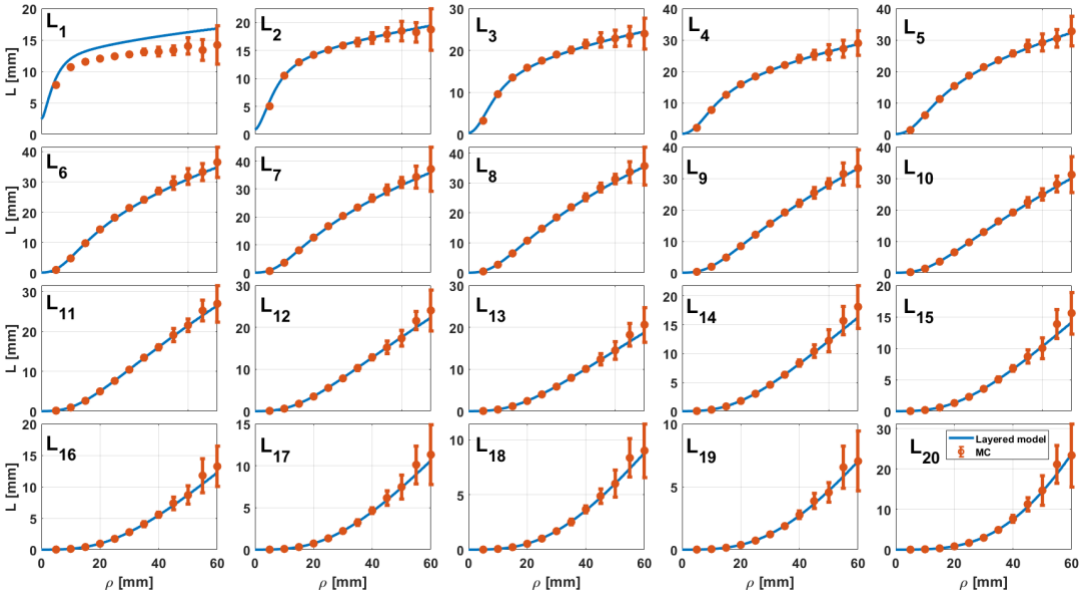

Fig. 10. Comparison (as a function of the source-detector distance ρ) between MC simulations and the analytical model of Section 2 for a twenty-layered medium, with optical properties $\boldsymbol{\mu}_a$ = (0.002, 0.015, 0.004, 0.010, 0.008, 0.003, 0.004, 0.002, 0.005, 0.006, 0.010, 0.013, 0.014, 0.013, 0.008, 0.007, 0.009, 0.007, 0.012, 0.011) mm^{-1} and $\boldsymbol{\mu}'_s$ = (1.10, 1.03, 0.82, 0.95, 0.78, 0.81, 0.85, 0.74, 1.06, 0.70, 0.89, 1.07, 0.93, 0.86, 1.02, 0.72, 0.76, 0.97, 0.91, 0.99) mm^{-1}, and the thicknesses being d_i = 1 mm, with i = 1,..., 19.

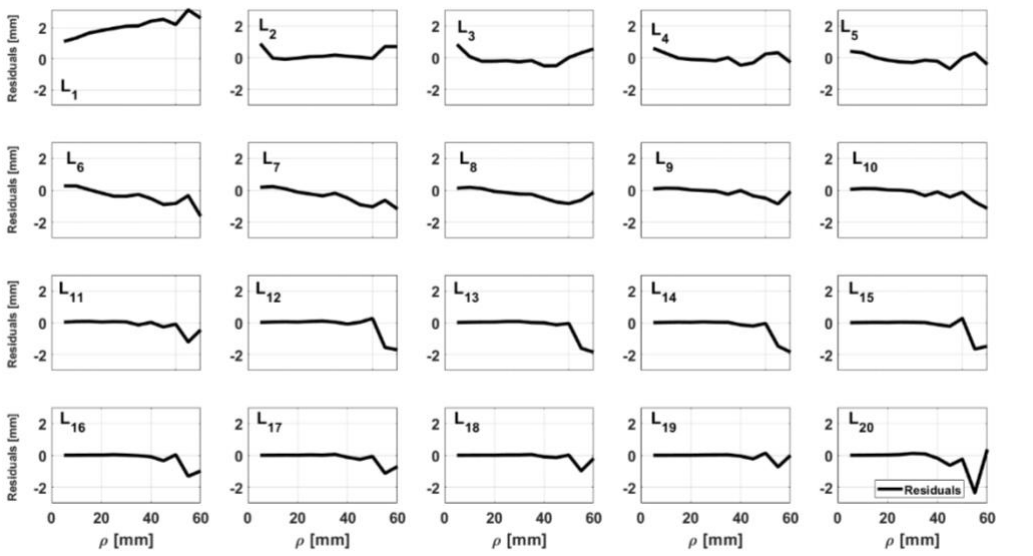

Fig. 11. Residuals obtained by subtracting the analytical MPPLs and the MC simulated MPPLs for the twenty-layered case.

Similarly to Fig. 7 for the ten-layered case, Fig. 11 shows the residuals that correspond to twenty-layered case. As mentioned before, and due to the same reasons, the largest differences are once again found in the first and last layers.

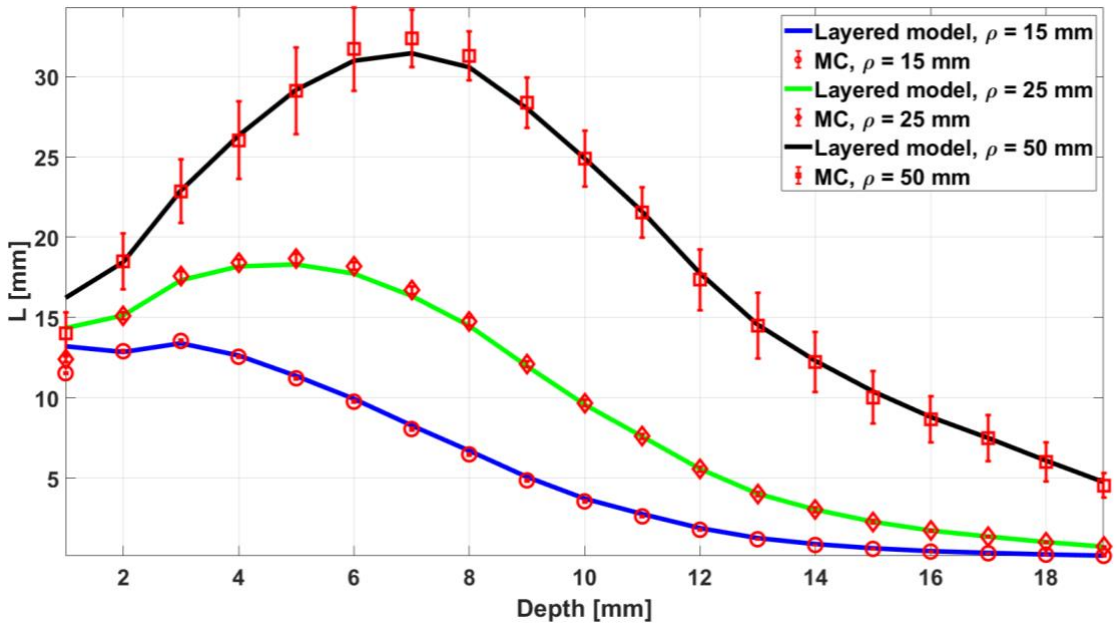

Fig. 12. Comparison between MC simulations and the MPPLs (as a function of the depth *z*) obtained by our analytical model for the twenty-layered medium shown in Fig. 9 and for three different source-detector distances, namely ρ = 15 mm, ρ = 25 mm and ρ = 50 mm.

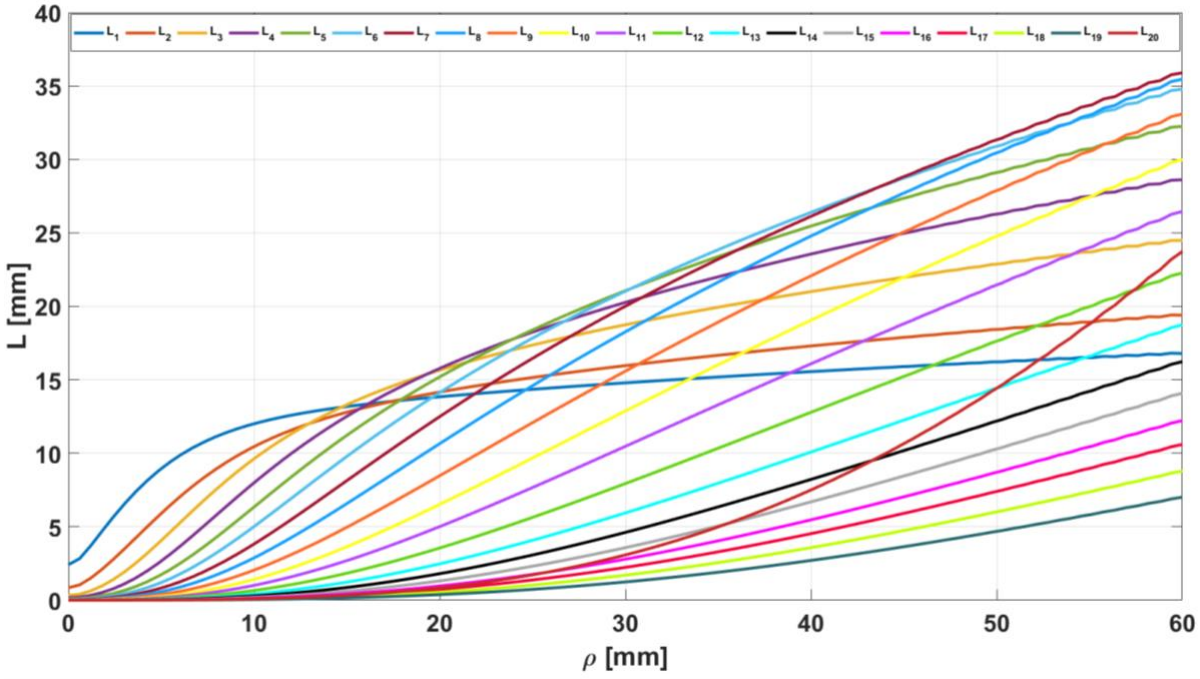

Fig. 13. Analytical MPPLs for the twenty-layered medium shown in Fig. 9, plotted altogether as a function of the source-detector separation ρ.

Finally, we must recall that one of the main applications of this work is the retrieval of (relative) haemoglobin concentration changes in cerebral blood. Current techniques mostly use homogeneous models to describe the human head (fast enough for real-time measurements, but rather far from reality); while few others compute the MPPLs in layered media by means of MC simulations (much more accurate than the homogeneous model, although impossible to be applied in real-time). Considering all this, we think that a theoretical model for the MPPLs that combines both advantages of the strategies just mentioned (i.e., the geometrical accuracy and the computational speed) with relative errors of less than 10% is, at least, a good compromise.

Furthermore, we can claim that going as far as to use a four-layered model greatly improves the reconstruction of relative absorption changes in layered media, when compared with the typical homogeneous reconstruction [32].

5. Conclusions

In this work, we have successfully obtained and implemented an analytical model for computing the MPPLs of photons in semiinfinite turbid media consisting in an arbitrary number of layers, which improves calculation times by several orders of magnitude (between 10^3 and 10^4) with respect to the most commonly used MC simulations and can be run under hardware requirements that are much less restrictive. This improvement will allow easy and real-time usage in experiments where brain haemodynamics, and particularly HbO and HbR concentration changes, are targeted.

Comparisons between our model and results generated with MC simulations are very encouraging, with relative differences below 10% for the first layer when large source-detector separations are used, and just in the extreme case of the twenty-layered medium. As already explained, it is thought that the reason for these differences is the lack of diffusiveness under these conditions, something difficult to overcome considering that our model is based on the diffusion approximation; hence, a next step would be to obtain analytical MPPLs in situations where the diffusive regime is not necessarily reached, which can be done by using the higher order approximations to the more general Radiative Transfer Equation [11,12]. As for the remaining results, in all cases the discrepancies lie below 5%, demonstrating that the model presented in this investigation can be reliably used to replace MC simulations for retrieving absorption changes [32] and, furthermore, haemoglobin concentration changes.

As a matter of fact, the external surface of the medium, as well as the internal interfaces between layers, have been assumed planar, i.e., the curvature is zero. However, the human head is better represented by a medium with spherical rather than a flat geometry. Although the source-detector distances investigated here (between 5 and 60 mm) are small compared to the average radius of the head, the head itself is not perfectly spherical, but presents regions of higher curvature (such as the transition between the forehead and the lateral and top areas, among others), which implies that, at some point, theoretical MPPLs for spherically shaped media could be necessary.

Nevertheless, we are certain that the current state of our model will still positively contribute to increasing the specificity of the measurements performed with any commercially available fNIRS acquisition device.

Acknowledgements

This work has been supported by CONICET (PIBAA 2022-2023 Nº 28720210100828CO) and by ANPCyT (PICT 2018 Nº 1295, PICT Start Up 2018 Nº 4709, PICT-2021-I-INVI-00125). We would like to thank Alejandro Díaz (MD) and María Inés García (MD) for their valuable comments and suggestions regarding the medical aspects of this investigation.